Wide Angle SAR Imaging

Randolph L. Moses[a], Lee C. Potter[a] and Mujdat Çetin[b],

[a]The Ohio State University, Department of Electrical and Computer Engineering
2015 Neil Avenue, Columbus, OH 43210, USA (moses.2@osu.edu, potter.36@osu.edu)
[b]Massachusetts Institute of Technology, Laboratory for Information and Decision Systems,
77 Massachusetts Ave, Cambridge, MA 02139 (mcetin@mit.edu)

ABSTRACT

We consider imaging strategies for synthetic aperture radar data collections that span a wide angular aperture. Most traditional radar imaging techniques are predicated on the assumption of isotropic point scattering mechanisms, which does not hold for wide apertures. We investigate point scattering center images for narrowband, wide angle data, and consider the effect of limited persistence on the resulting images. We investigate imaging strategies that apply to wide angle apertures. We show that coherent processing of the entire wide angle aperture may not be the best image formation strategy for objects of practical interest. Finally, we present initial results on resolution enhancement techniques for wide angle apertures.

Keywords: synthetic aperture radar, wide angle, radar imaging

1. INTRODUCTION

Wide-angle synthetic aperture radar (SAR) refers to any synthesized aperture whose angular extent, $\Delta\phi$, exceeds the sector required for equal resolution in range and cross-range:

$$\Delta\phi > 2\sin^{-1}\left(BW/(2f_c)\right) \tag{1}$$

where BW and f_c are the bandwidth and center frequency of the radar. For X-band systems, which operate near $f_c = 10\,\text{GHz}$, Table 1 lists the aperture sizes to give equal downrange and crossrange resolution for several radar bandwidths.

A number of recent technology advancements enable consideration of wide angle imaging. First, advancements in GPS and INS systems permit collection of coherent data across longer times and flight paths. Second, unmanned air vehicle (UAV) technology and collaboration among UAVs provide a number of wide angle imaging possibilities. UAVs can in many applications fly closer to the scene of interest, and thus can traverse a wider angle aperture in a given amount of time compared to a platform with a greater standoff distance. Bistatic radar scenarios, in which a distant standoff platform acts as the transmitter and one or more UAVs act as closer-in receivers, can also provide greater angular coverage. UAVs working in tandem can collect angular subapertures which can then be combined into a wider aperture. As we discuss in Section 3, phase coherence of these subapertures may not be necessary for effective wide-angle imaging.

Wide angle imaging presents a number of technical challenges. First, many existing algorithms for radar imaging implicitly or explicitly assume that the measured data lies on a filled rectilinear grid in frequency space. In wide angle imaging applications, this assumption becomes unrealistic. Second, much of the radar imaging literature assumes that scattering from objects of interest can be modeled (at least in part) as a set of isotropic point scattering centers. For narrow angular apertures, this assumption is often appropriate; however, for wide angle apertures, the angle-dependent amplitude of scattering returns become significant.

In spite of these technical challenges, wide angle imaging offers significant potential advantage for object recognition and visualization. Because radar returns are often dominated by specular returns on the object, many radar images have a response in which a few bright points dominate the image. In contrast, optical images contain significant diffuse scattering components, providing "fill" to the images. Wide angle SAR imaging offers the potential of combining specular returns over a wide angle to provide more of a diffuse-like image that is more readily recognized and interpretable by humans.

Table 1. Nominal aperture size for equal downrange and crossrange resolution at X-band with $f_c = 10$ GHz.

bandwidth (MHz)	resolution (cm)	resolution (inches)	aperture (degrees)
500	30	11.8	2.87
1000	15	5.9	5.73
2000	7.50	3.0	11.48
4000	3.75	1.5	23.07

Wide-angle imaging measures scattering behavior that can differ significantly from the behavior observed, for example, with 30 cm resolution X-band data. For typical ground targets, the aspect-dependent behavior of scattering components may vary drastically across a wide-angle aperture due to shadowing, scintillation, and non-point-like geometry. In this paper we consider imaging algorithms that accommodate such aspect-dependent scattering behavior.

An outline of this paper is as follows. In Section 2 we present some results on wide angle imaging image responses for ideal point scattering centers and for scattering centers whose response persists over a subset of the measurement aperture. In Section 3 we discuss how scattering physics suggests image formation techniques that deviate from traditional coherent image formation. We then present imaging results obtained from synthetic frequency-domain scattering predictions of a vehicle. In Section 4 we discuss methods for resolution enhancement in wide angle imagery, and present initial results using a regularized inverse imaging process. Section 5 presents some conclusions and suggestions for future research.

2. WIDE ANGLE IMAGING

2.1. EM Scattering

Electromagnetic scattering from a scene may be fully described as a function of spatial location, viewing geometry, frequency and polarization. For monostatic data collection, the scattered electric field from an object can be described by a 2-by-2 polarimetric scattering matrix, Ψ

$$\Psi\left(x, y, z, f, \phi, \theta\right) \tag{2}$$

where (x, y, z) is the object location, f is frequency, and (ϕ, θ) describe the monostatic azimuth and elevation viewing angles. For example, creeping waves, cavities and diffraction each cause a non-uniform behavior as a function of frequency; likewise, dihedrals and shadowing, for example, both result in a non-isotropic angular response. The measured fields are modeled by

$$E(f, \phi) \approx \int_{x,y} \frac{1}{\|r - r_m\|^2} \Psi\left(x, y, z, f, \phi, \theta\right) E_i \exp\left\{ j2\pi f \frac{\|r_m - r\| - \|r_m\|}{c/2} \right\} \tag{3}$$

where r_m is the location of the mth aperture sample, $r = [x, y, z]$, and $E_i \in C^2$ is the incident field. In this superposition model, only backscatter is modeled; the scattered fields that impinge on neighboring objects are not included in the approximation. Thus, the interactions of scene components must be accounted for by modification of the frequency and angle dependence of Ψ.

Imaging is a two-dimensional representation formed from the multi-variable function Ψ. Consequently, some behaviors may be obscured. Adopting a linear aperture leaves unresolvable any scene displacement from the slant plane; thus, viewing position may be parameterized by one angle and location by two variables. In addition, with a narrow-band assumption, we eliminate the frequency variable to arrive at

$$\Psi\left(x, y, \phi\right) \tag{4}$$

Most imaging approaches further abandon the angle dependence, yielding a function of two variables readily depicted as a two-dimensional map

$$\Psi\left(x, y\right) \tag{5}$$

Finally, a far-field plane-wave propagation assumption yields a linearization of the differential range, $\|r_m\| - \|r\|$

$$E(f,\phi) = \int_{x,y} \Psi(x,y)\, E_i \exp\left\{ j2\pi f \cos\theta \frac{(x\cos\phi + y\sin\phi)}{c/2} \right\} \tag{6}$$

The plane wave assumption simplifies Fourier processing,[1] but results in a predominantly quadratic phase error due to wavefront curvature; this error is limited by restricting the image scene size to be small relative to the stand-off distance.

With the unavoidable warping of a high-dimensional scattering behavior onto a two-dimensional map, the question arises: what is a SAR image? The inevitable answer is that a SAR image must be a data format suitable for *use*; yet, this answer serves only to beg the precise definition of the use. We will explore this question in the context of wide angle imagimg of a vehicle in Section 3.

2.2. Resolution Enhancement of Wide Angle Apertures

An enticing characteristic of wide-angle data is bandwidth enhancement. For example, consider the 90 degree aperture with 500 MHz bandwidth shown in Figure 1. The maximum extent of samples in the f_x and f_y spatial frequencies are

$$\begin{aligned} \max\{f_x\} - \min\{f_x\} &= (f_c + BW/2) - f_c\cos(90/2) = 3.18 \text{ GHz} \\ \max\{f_y\} - \min\{f_y\} &= 2\,(f_c + BW/2)\sin(90/2) = 14.50 \text{ GHz} \end{aligned} \tag{7}$$

This bandwidth expansion factors are approximately 6 in range and 29 in cross-range, compared with the 500 MHz radar bandwidth. This bandwidth enhancement is evidenced in the image point response (IPR) plots given in Figure 2. The images are formed by polar separable Taylor windowing (-35 dB, nbar=4), interpolation to cartesian grid points lying within the annular support, then a zero-padded fast Fourier transform. In the left column, we see the 6 dB peak contours for the 2.87 degree (1 foot resolution, as in MSTAR) and 90 degree apertures. In the right column, we see the corresponding images. The 6 dB areas are approximately 1619 cm^2 and 24 cm^2. This is a ratio of approximately $67:1$, which is about 40% of the bandwidth enhancement, despite the sparse aperture that fills only 15.6% of the circumscribing rectangle. However, comparison of the 24 dB contours shows only a $9.5:1$ reduction in main lobe area. For further comparison, Figure 3 shows IPRs for a fully filled outer rectangle and a square rectangular with area equal to the 90 degree, 500 MHz annulus.

Thus, the wide-angle data collection dramatically enhances the -6 dB resolution in both range and cross-range; however, the improvement at the -24 dB level is less significant.

Alternative windowing strategies can only offer minor changes to an IPR with very small -6 dB resolution but relatively broad side lobes. The improvement is ultimately limited by the time-frequency uncertainty principle, which is a consequence of the Cauchy-Schwarz inequality.

Moreover, IPR plays a less central role in wide-angle imaging than in narrow-angle SAR because few, if any, reflectors have a point-like response across the full aperture. From studies of scattering persistence,[2] strong reflectors will appear as a mixture of narrow angle responses, such as 2 to 5 degrees, with a few reflectors persisting across 10 to 20 degrees. We note that results of empirical studies such as this one are likely to be dependent on the radar resolution due to scintillation of unresolved scattering mechanisms; we expect to see larger average persistence angles for higher resolution data. Further, an image that coherently combines scattering returns from across the entire aperture may obscure aspect-dependent behavior characterizing target scattering. For these reasons, procedures other than full aperture polar format or wavefront image formation processing methods may be desirable, as discussed in Section 3.

Figures 4 and 5 show the frequency support and corresponding image response of point scattering mechanisms for various persistence angles and various peak response azimuths. Note from Figure 4 that the scattering persistence must be large before downrange resolution enhancement begins to appear; the downrange extent of the frequency support is

$$\left(f_c + \frac{BW}{2}\right) - \left(f_c - \frac{BW}{2}\right)\cos(\Delta\phi/2) \approx BW + \frac{f_c\Delta\phi^2}{8} \tag{8}$$

(assuming $BW \ll f_c$ and using the Taylor series approximation $\cos\phi \approx 1 - \phi^2/2$). For a 5% bandwidth radar (such as a 500 MHz bandwidth radar with center frequency of 10 GHz), then from equation (8) one needs an aperture of $\Delta\phi = 36°$ to increase the downrange resolution by a factor of two. However, evidence suggests that few scattering centers will persist for this large an aperture. Figure 5 shows the image responses for a 20° scattering persistence for various peak response azimuths; for this aperture, the downrange bandwidth given in equation (8) is about 30% higher than the redar bandwidth.

3. WIDE ANGLE SCATTERING PHYSICS AND IMAGING OF TARGETS

For many years, technology has restricted apertures and bandwidths such that the point scattering assumption can serve as a good approximation. Small fractional bandwidth and narrow aperture mean that frequency and aspect dependent behavior are not observed in the measured data. For wide angle and/or large fractional bandwidths, the point scattering assumption may no longer hold. Consequently,[3]

> *...the electromagnetic notion of a point scatterer is, arguably, more of a mathematical and conceptual construct than a physically meaningful entity. The usual purpose and role of SAR imaging is far more complicated than the simple problem of estimating optimally the location of and amplitude of point scatterers.* (DeGraaf, 1998, page 742)

To illustrate this point, we consider wide angle images formed from XpatchF data of a backhoe, shown in Figure 6. Images were formed from a linear aperture with an azimuth extent of 110° and a peak elevation angle (at azimuth center $\phi_c = 45°$) of $\theta_c = 30°$. The formula for (az,el)=(ϕ, θ) angle pairs to simulate a horizontal linear aperture with center azimuth and elevation of (ϕ_c, θ_c) is given by:

$$\theta(\phi) = \tan^{-1}\left[\cos(\phi - \phi_c) \cdot \tan(\theta_c)\right] \tag{9}$$

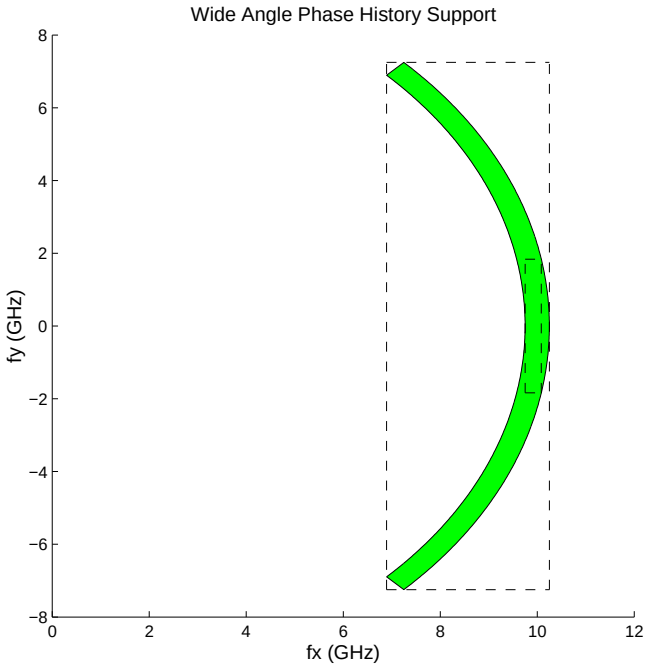

Figure 1. Region of support for wide-angle phase history measurements. In the example, $f_c = 10\,\text{GHz}$, bandwidth is 500 MHz, and the aperture subtends 90 degrees at broadside squint. The dashed rectangles depict the inscribed and circumscribed rectangular support regions.

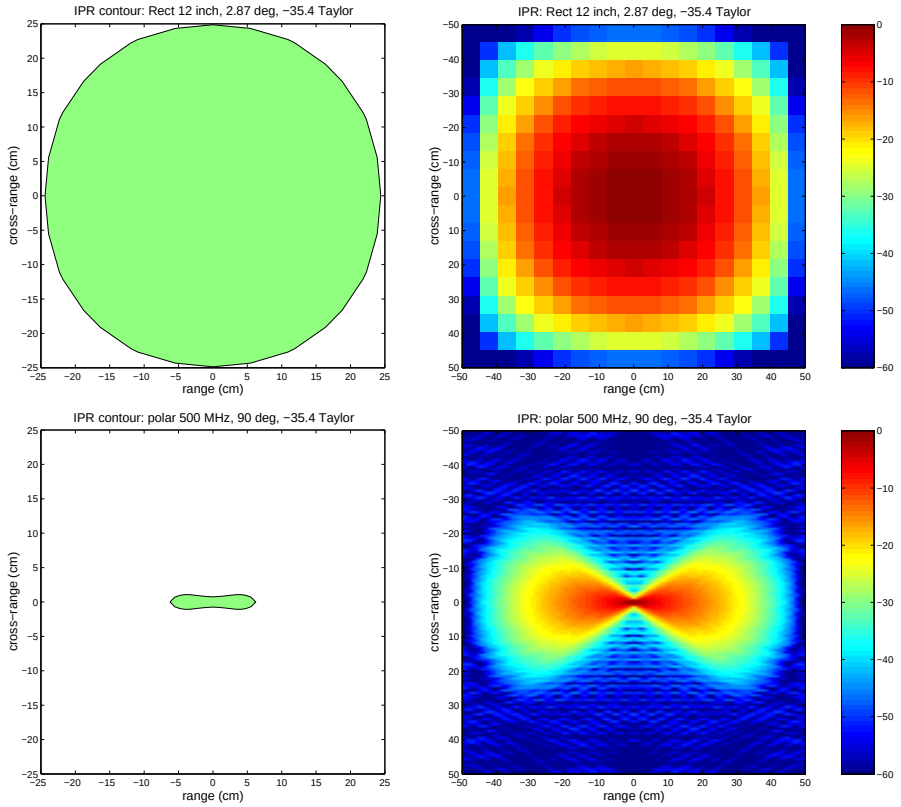

Figure 2. Wide-angle data provides bandwidth enhancement. Left: -6 dB contour of the IPR for 500 MHz bandwidth, 5.87 degree aperture (top) and 90 degree aperture (bottom). The corresponding IPRs are shown in the right column. Note the right column images depict 1 m^2, and the left column images display 0.25 m^2.

For each image, a center frequency of $f_c = 10$ GHz was used, and bandwidths of 4 GHz and 500 MHz were used. The resulting images are shown in Figure 7. The 500 MHz image shows most scattering mechanisms as oriented narrow ellipsoids, indicative of aspect-dependent scattering (compare to the response images in Figure 5).

Full-aperture images such as those in Figure 7 may not be the best representation of scattering behavior. An interpretation of unwindowed Fourier imaging is a matched filter for a single point scatterer in additive white Gaussian noise.[4] Thus, full-aperture images can be interpreted as matched filtering to an *isotropic* point scattering center (whose response persists over the entire aperture). However, most scattering mechanisms have a response over a much narrower aperture. The matched filter corresponding to full-aperture imaging is not well-matched to most scattering behavior on the object. As a result, a large amplitude scattering term that persists over a narrow angle may appear as a low-amplitude response in the image, because the image averages the response over the entire wide-angle azimuth aperture.

An alternate approach is to use a bank of matched filters, each characterized by a center response azimuth and a response width and shape.[5,6] As a computationally-efficient surrogate that illustrates this approach, we quantize this filter bank by a set of 19 filters, each matched to a scatterer with an azimuth response centered at 0°, 5°, ..., 90°. The response width and shape are chosen to be a a Hamming window of width 20°. Future work could consider more complete quantizations of the filter bank space. Each of these matched filter outputs is a subimage formed by using a 20° subaperture of the full azimuth aperture.

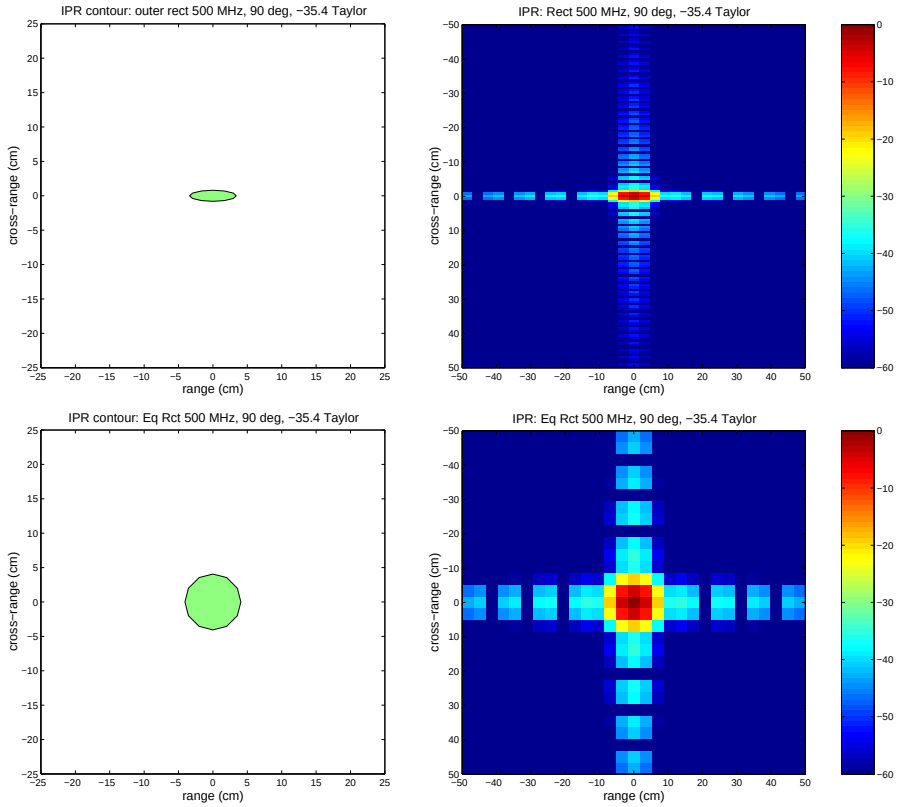

Figure 3. The −6 dB IPR contours and IPR magnitude images for the circumscribed rectangular region of support (top row) and the square region of support of area equal to the wide-angle annulus (bottom row). Note the right column images depict $1\,\mathrm{m}^2$, and the left column images display $0.25\,\mathrm{m}^2$.

Figure 8 shows the composite output of the matched-filter images. In the composite image, the filter output (*i.e.,* subimage) with the maximum pixel magnitude is retained. Thus, pixel p_{ij} is defined as:

$$p_{ij} = \arg\max_k p_{ij}^k \approx \arg\max_{\phi_p} p_{ij}^{\phi} \tag{10}$$

where p_{ij}^k is the i,jth pixel of subimage k, which is, assuming a sufficiently fine quantization of the filter bank space, the maximum pixel over all filter outputs p_{ij}^{ϕ} whose scattering response peaks at angle ϕ_p. Thus, the composite image has the interpretation of a Generalized Likelihood Ratio Test (GLRT) statistic for scattering responses with known response shape[5,6] (in this case, Hamming with persistence width of 20°) but with unknown peak response angle. We note that additional information which is available, but not shown, for each pixel is the index k of the corresponding subimage at which the maximum occurs. This index information may be useful for aiding object visualization or for use in an automatic target recognition algorithm, and is a topic of current study.

Comparing Figure 8 with the coherent image of Figure 7, we see larger response amplitudes for narrow-aperture scattering centers, and generally better "fill" from which to observe the object shape. In addition, the resolution of the full-aperture image appears to be no better than that in the composite image, another indication that resolution in this case is limited by scattering response persistence and not by coherent aperture width.

It is important to note that the images obtained in Figure 8 are obtained by *non-coherent* combinations of 20° subaperture images. Thus, effective wide angle image formation does not require radar signal coherence across the entire wide angle aperture. In particular, the subapertures could be obtained from separate radar platforms and then combined.

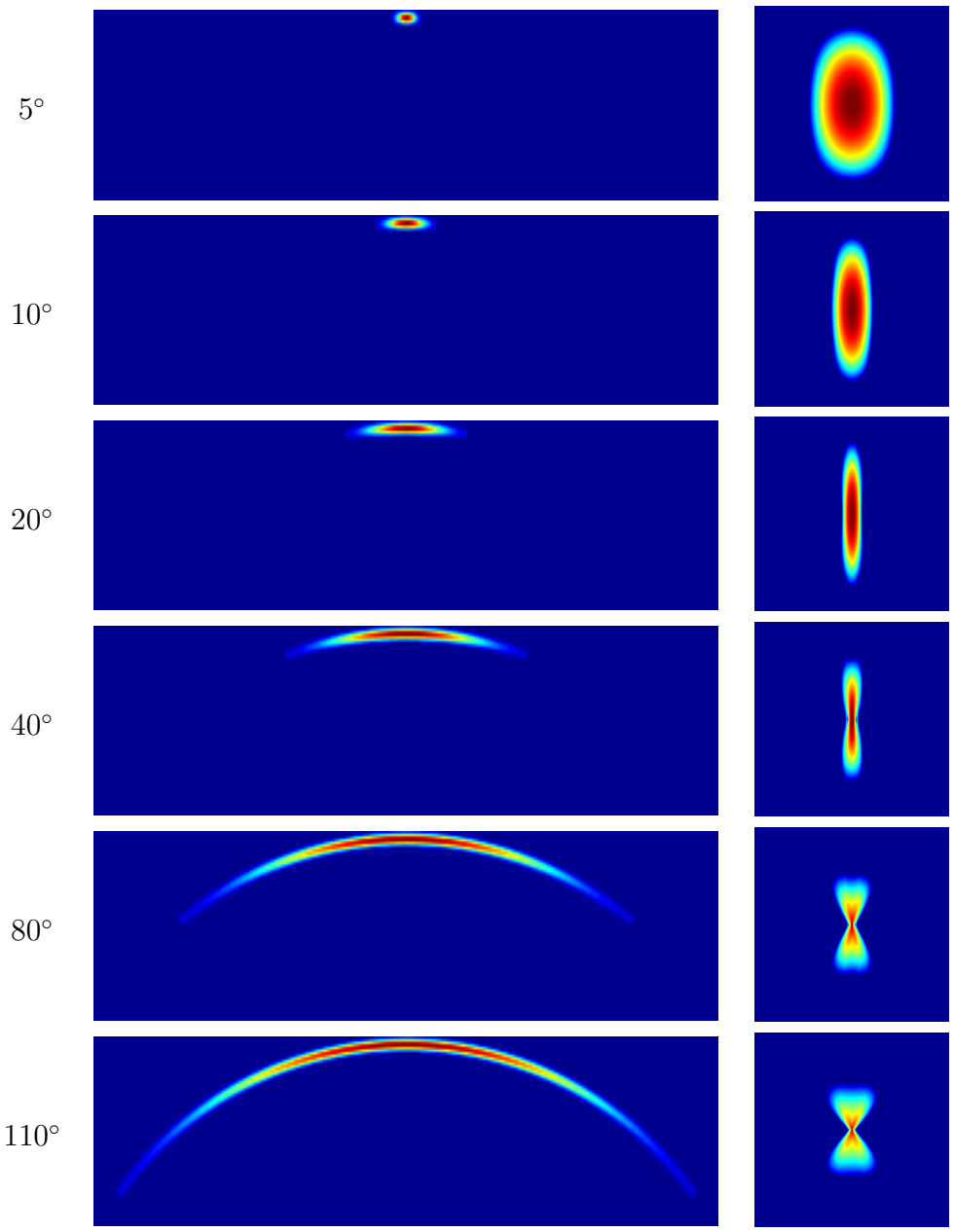

Figure 4. Frequency support (left) and image for a point scattering center with varying persistence angles. The frequency support region is 5.4×18.0 GHz, and the images are 2×2 meters. The images are in logarithmic scale and show the top 40 dB of the responses.

4. RESOLUTION-ENHANCED IMAGE FORMATION

Narrowband, wide angle images such as those in Figures 7(b) and 8(b) exhibit crossrange resolution that is limited by scattering persistence, and downrange resolution (where in this case downrange is in the direction defined by the peak response azimuth of a given scattering center) defined by the radar bandwidth. In this section we present initial results of applying resolution enhancement algorithms to improve resolution, especially in the downrange direction.

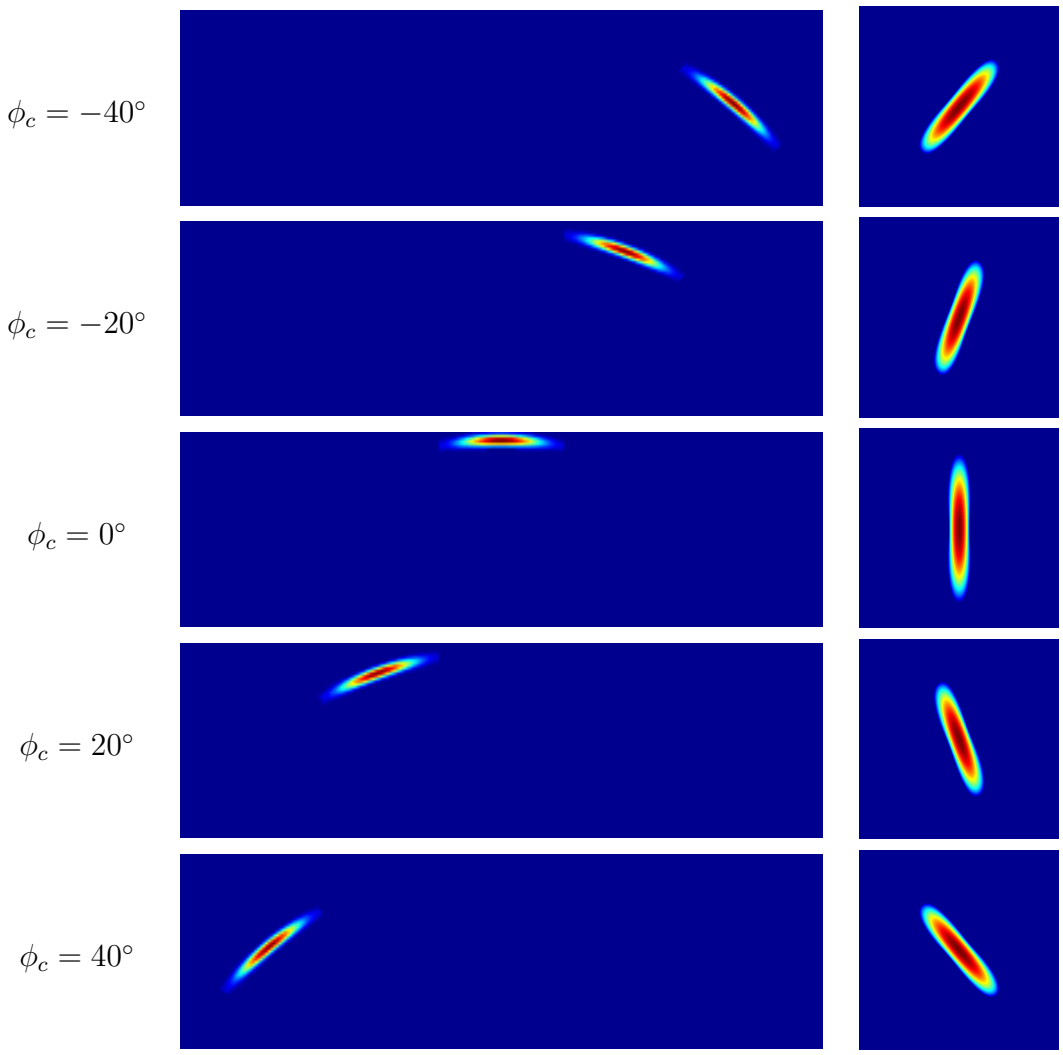

Figure 5. Frequency support (left) and image for a point scattering center with varying persistence angle of 20◦ and varying peak response center azimuth angle ϕ_c. The frequency support region is 5.4×18.0 GHz, and the images are 2×2 meters. The images are in logarithmic scale and show the top 40 dB of the responses.

A number of techniques have been proposed for resolution enhancement in radar imagery, including filter bank methods,[3,7–9] linear prediction based methods such as AR modeling, MUSIC or ESPRIT (see Degraaf[3] for a survey of linear prediction based methods), parametric[10–17] and semiparametric[18] model fitting methods, and regularized inverse methods.[19–22] Many of these techniques were derived for narrowband, narrow angle radar measurements, and are not immediately applicable to wide angle data. For example, many of these techniques assume point scattering models (either implicitly or explicitly) or assume equally-spaced rectilinear data frequency space.

As an initial study on the effectiveness of resolution-enhanced image formation, we adopt a regularized l_p-norm based method proposed by Çetin and Karl,[21] which has been applied successfully to radar imagery. The algorithm is nonparametric and thus somewhat robust to scattering physics assumptions.

For ideal point reflectors located on the slant plane, Equations (2) and (5) are equivalent, and a discretization of the xy-plane reduces Equation (3) to a linear system of equations relating the measurements to the unknown

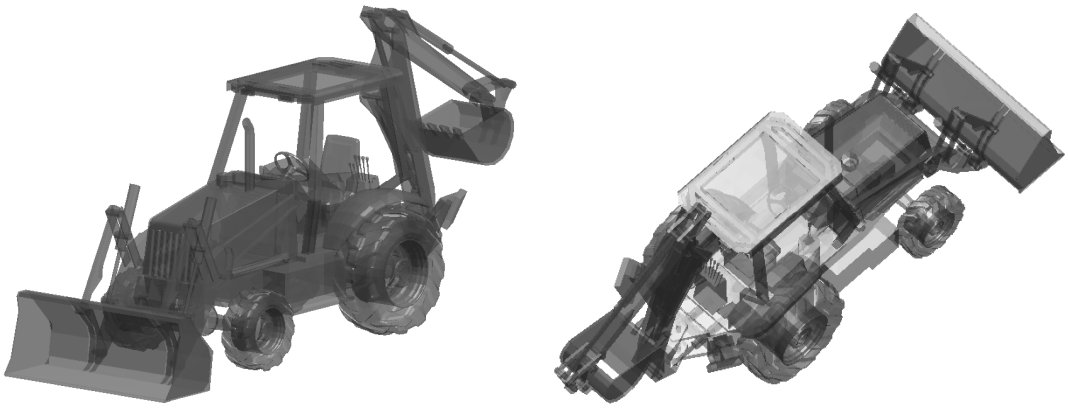

Figure 6. Backhoe model used in Xpatch scattering predictions. The view to the right corresponds approximately to the images in Figures 7–9.

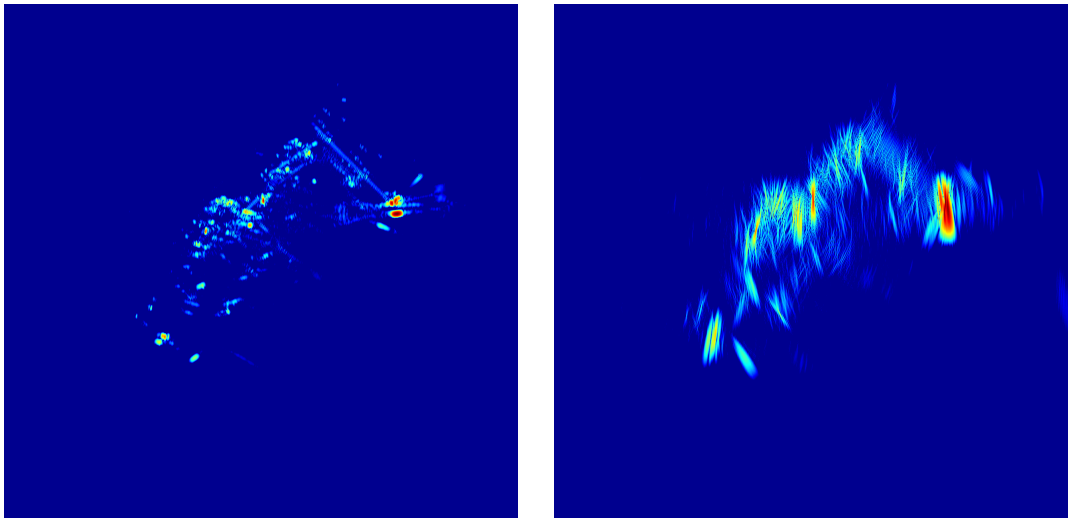

(a) (b)

Figure 7. SAR image of the backhoe using a 110° linear aperture centered at 45° azimuth and 30° elevation. (a) 4 GHz frequency bandwidth (1.5 inch resolution) image. (b) 500 MHz frequency bandwidth (1 ft inch resolution) image.

scene

$$Au = b. \tag{11}$$

Here b are (noisy) samples of the measured phase history $E(f, \phi)$, u is the discretized grid of unknown point scattering amplitudes and phases, and A is given by discretization of the integral in Equation (3). The matrix A is determined by the aperture and the scene center. Direct least-squares solution of Equation (11) is given by

$$\hat{u} = A^{\dagger} b \tag{12}$$

where $A^{\dagger}$ denotes the pseudo-inverse. If Equation (11) is under-determined, $A^{\dagger}$ yields the least-squares solution of minimum norm.

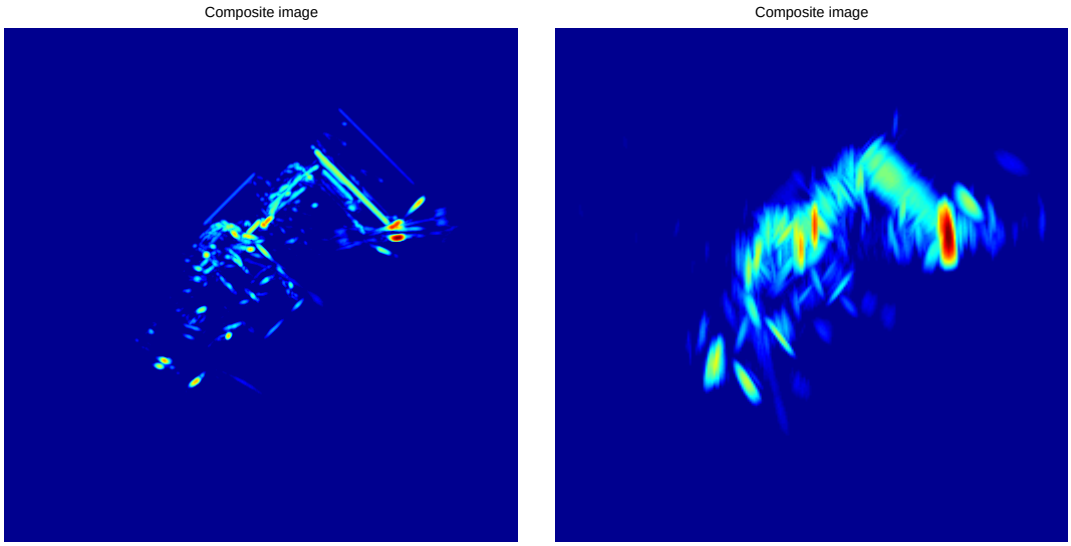

(a) (b)

Figure 8. Composite Matched filter SAR image of the backhoe using a 110° linear aperture centered at 45° azimuth and 30° elevation, for scattering responses with persistence 20° and Hamming response shape. (a) 4 GHz frequency bandwidth (1.5 inch resolution) image; (b) 500 MHz frequency bandwidth (1 ft inch resolution) image.

The least-squares solution for Equation (11) has desirable properties, *e.g.*, maximum likelihood for additive white Gaussian measurement noise. However, the computational complexity of the pseudo-inverse is high; it is $O(N^6)$ in the common situation that numbers of frequency and aperture samples and the number of pixels in the x and y directions are each $O(N)$.

In the l_p-norm techniques, imaging is formulated as the inverse to a large linear system in Equation (11). The matrix A encodes a discretized model for the scattering behavior; typically, point scattering is used. For image enhancement of linear phase scattering centers, point-like solutions are sought for the under-determined set of linear equations; l_p-norms, for $p \leq 1$, provide a means for achieving sparse solutions (and are used, for example, in basis selection literature).

Generally, the l_p-norm techniques solve the optimization problem of the form

$$\min_u \left\{ \|Au - b\|^2 + \lambda \|u\|_p^p \right\} \tag{13}$$

Here, $\|\cdot\|_p^p$ denotes the pth power of the p-norm. Equation (13) may be viewed as a regularization of $Au = b$, in which fidelity to the measured (noisy) phase history is traded against the l_p "energy" penalty.

We note that the above solution is predicated on a point scattering assumption, which does not hold for wide angle apertures. However, the point scattering assumption is reasonable over subapertures of sufficiently small size. Thus, we apply l_p-norm enhancement to subimages of the wide-angle aperture.

Figure 9 shows the results of the above l_p-norm image formation with $\lambda = 1$ and for $p = 1$ and $p = 0.8$. In these figures, an l_p subaperture image was first formed for each subaperture used in Figure 8. Then, these l_p subimages were used to form a composite image using equation (10) and are analogous to Figure 8(b). The choice of $p = 0.8$ favors sparse solutions more than when $p = 1$, so the $p = 0.8$ composite image shows more point-like sharpening. In both composite images, we see significant improvement in the downrange resolution, as well as some sharpening in the crossrange (compare to Figure 8(b)). Although these l_p-composite images are based on the same low-bandwidth data used for the images in Figures 7(b) and 8(b), they appear to exhibit some of the features present in the images in Figures 7(a) and 8(a), which use eight times the bandwidth.

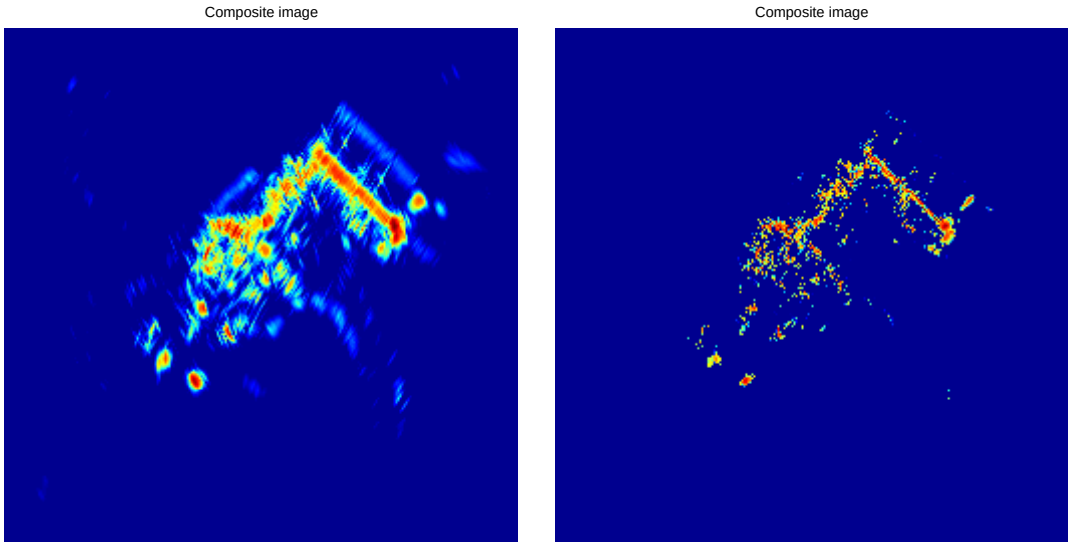

(a) $p = 1$, $\lambda = 0.1$ (b) $p = 0.8$, $\lambda = 0.1$

Figure 9. Composite Matched filter SAR image of the backhoe using 500 MHz radar bandwidth, after applying l_p-norm resolution enhancement with $p = 1$ and $p = 0.8$.

5. CONCLUSION

We have considered aspects of wide angle synthetic aperture radar imaging. Traditional SAR imaging techniques often assume rectangular or near-rectangular frequency-domain data and are based on a point scattering assumption; neither holds true in the wide angle imaging case. While coherent, wide-angle image formation results in a high-resolution impulse response, limited persistence of scattering centers effectively limits the observed resolution. We have proposed a composite nonlinear combination of subaperture images as an alternative to coherent imaging over a wide aperture; the subaperture combination has the interpretation of a generalized likelihood ratio test (GLRT) for matched filtering of scattering responses with unknown peak azimuth response direction. Using this approach, wide-angle composite SAR images are obtained by *noncoherent* combination of narrower-aperture subimages. Finally, we briefly explored the use of regularized inverse imaging solutions, and showed by example that substantial resolution enhancement is possible using narrowband, wide angle data.

Future work will consider scattering persistence behavior in more detail and derive corresponding matched filter and GLRT image formation techniques that are better matched to this behavior than the preliminary examples presented here. In addition, resolution enhancement that is better matched to the narrow bandwidth, wide aperture data measurements will be considered. Finally, use of scatterer response angle as a visualization tool or target recognition statistic will be studied.

ACKNOWLEDGMENTS

The authors would like to thank Ed Zelnio, Mike Minardi, and Ron Dilsavor at Air Force Research Laboratory for many fruitful discussions on wide angle imaging. We would also like to thank SAIC for providing XpatchF scattering predictions of the backhoe.

REFERENCES

1. C.V. Jakowatz, D.E. Wahl and P.H. Eichel, *Spotlight-Mode Synthetic Aperture Radar: A Signal Processing Approach*, Kluwer Academic Publishers, Boston, MA, 1996.
2. D. E. Dudgeon, R. T. Lacoss, C. H. Lazott, and J. G. Verly, "Use of persistant scatterers for model-based recognition," in *Algorithms for Synthetic Aperture Radar Imagery (Proc. SPIE 2230)*, D. A. Giglio, ed., pp. 356–368, April 1994.

3. S. DeGraaf, "SAR imaging via modern 2-D spectral estimation methods," *IEEE Transactions on Image Processing* **7**, pp. 729–761, May 1998.
4. D. Rossi and A. Willsky, "Reconstruction from projections based on detection and estimation of objects–Parts I and II: Performance analysis and robustness analysis," *IEEE Transactions on Acoustics, Speech, and Signal Processing* **32**, pp. 886–906, August 1984.
5. M. R. Allen and L. E. Hoff, "Wide-angle wideband SAR matched filter image formation for enhanced detection performace," in *Algorithms for Synthetic Aperture Radar Imagery*, **2230**, pp. 302–314, SPIE, (Orlando FL), April 1994.
6. R. D. Chaney, A. S. Willsky, and L. M. Novak, "Coherent aspect-dependent SAR image formation," in *Algorithms for Synthetic Aperture Radar Imagery*, **2230**, pp. 256–274, SPIE, (Orlando FL), April 1994.
7. P. Stoica, H. Li, and J. Li, "A new derivation of the APES filter," *IEEE Signal Processing Letters* **6**, pp. 205–206, August 1999.
8. G. R. Benitz, "High-definition vector imaging," *Lincoln Laboratory Journal* **10**(2), pp. 147–170, 1997.
9. E. G. Larsonn, G. Liu, P. Stoica, and J. Li, "High-resolution SAR imaging with angular diversity," *IEEE Transactions on Aerospace and Electronic Systems* **37**, pp. 1359–1372, October 2001.
10. S. DeGraaf, "Parametric estimation of complex 2-D sinusoids," Tech. Rep. OSL-90-6383, ERIM, Ann Arbor, MI, 1990.
11. J. J. Sacchini, W. M. Steedly, and R. L. Moses, "Two-dimensional Prony modeling and parameter estimation," *IEEE Transactions on Signal Processing* **41**, pp. 3127–3137, November 1993.
12. M. P. Pepin and J. J. Sacchini, "Maximum likelihood estimation of point scatterers in synthetic aperture radar data," in *Proc. IEEE National Aerospace and Electronics Conference (NAECON 1996)*, **1**, pp. 68–74, May 1996.
13. Y. Hua, "Estimating two-dimensional frequencies by matrix enhancement and matrix pencil," *IEEE Transactions on Signal Processing* **40**, pp. 2267–2280, September 1992.
14. M. J. Gerry, L. C. Potter, I. J. Gupta, and A. van der Merwe, "A parametric model for synthetic aperture radar measurements," *IEEE Transactions on Antennas and Propagation* **47**, pp. 1179–1188, July 1999.
15. B. Rigling, *Signal processing strategies for bistatic synthetic aperture radar*. PhD thesis, Ohio State University, http://www.ohiolink.edu/etd/, 2003.
16. Z.-S. Liu and J. Li, "Feature extraction of SAR targets consisting of trihedral and dihedrals corner reflectors," *IEE Proceedings: Radar, Sonar and Navigation* **145**, pp. 161–172, March 1998.
17. L. C. Trintinalia, R. Bhalla, and H. Ling, "Scattering center parameterization of wide-angle backscattered data using adaptive Gaussian representation," *IEEE Transactions on Antennas and Propagation* **45**, pp. 1664–1668, November 1997.
18. R. Wu, J. Li, Z. Bi, and P. Stoica, "SAR image formation via semiparametric spectral estimation," *IEEE Transactions on Aerospace and Electronic Systems* **35**, pp. 1318–1333, October 1999.
19. A. E. Brito, S. H. Chan, and S. Cabrera, "SAR image formation using 2-D reweighted minimum norm extrapolation," in *Algorithms for Synthetic Aperture Radar Imagery VI (SPIE vol. 3721)*, pp. 78–91, April 1999.
20. A. E. Brito, S. Cabrera, and C. Villalobos, "Optimal sparse representation algorithms for harmonic retrieval," in *Thirty-Fifth Asilomar Conference on Signals, Systems and Computers*, pp. 1407–1411, November 2001.
21. M. Çetin and W. C. Karl, "Feature enhanced synthetic aperture radar image formation based on nonquadratic regularization," *IEEE Transactions on Image Processing* **10**, pp. 623–631, April 2001.
22. B. D. Rao and K. Kreutz-Delgado, "An affine scaling transformation for best basis selection," *IEEE Transactions on Signal Processing* **47**, pp. 187–200, January 1999.